Mühendislik Bilimleri ve Tasarım Dergisi
13(4), 1034-1046, 2025
e-ISSN: 1308-6693

Journal of Engineering Sciences and Design
DOI: 10.21923/jesd.1706211

Araştırma Makalesi Research Article

CHARACTERIZATION OF THE SURFACE TOPOGRAPHY OF THE TI-6AL-4V ALLOY FABRICATED BY LASER POWDER BED FUSION

Samira MOHAGHEGHI[1*]

[1]İstinye University, Faculty of Engineering and Natural Sciences, Department of Mechanical Engineering, İstanbul 34408, Türkiye

Keywords

Additive Manufacturing, Laser Powder Bed Fusion, Ti-6Al-4V, Surface Roughness.

Abstract

Laser powder bed fusion (L-PBF) is a class of additive manufacturing processes in which a high-energy laser selectively melts layers of metallic powder to fabricate three-dimensional components. While L-PBF enables significant advancements in the manufacturing of complex geometries, poor surface quality of the as-built parts is still a drawback of the process. High surface roughness in as-built parts is primarily caused by the complex thermal history during the melting, solidification, and cooling processes. In this study, rectangular samples were fabricated from Ti-6Al-4V powder by the L-PBF process. Surface topography of the samples in as-build state, both top and side surfaces, was characterized using a surface roughness tester and a scanning electron microscope (SEM). The origins of surface roughness were found to differ significantly between the two orientations. On the side surfaces, roughness is predominantly due to the attachment of partially melted powder particles. In contrast, the top surface roughness is influenced by several defects, with balling phenomena playing a major role in generating highly rough surfaces.

LAZER TOZ YATAK FÜZYONU İLE ÜRETİLEN TI-6AL-4V ALAŞIMININ YÜZEY TOPOGRAFYASININ KARAKTERİZASYONU

Anahtar Kelimeler

Eklemeli İmalat, Lazer Toz Yatak Füzyon, Ti-6Al-4V, Yüzey Pürüzlülüğü.

Öz

Lazer toz yatağı füzyonu (L-PBF), yüksek enerjili bir lazerin üç boyutlu bileşenler üretmek için metalik toz katmanlarını seçici olarak ergittiği bir eklemeli üretim süreci sınıfıdır. L-PBF karmaşık geometrilerin üretiminde önemli ilerlemeler sağlarken, üretilen parçaların düşük yüzey kalitesi hala sürecin bir dezavantajıdır. Üretilen parçalardaki yüksek yüzey pürüzlülüğü temel olarak eritme, katılaştırma ve soğutma süreçleri sırasındaki karmaşık termal geçmişten kaynaklanmaktadır. Bu çalışmada, Ti-6Al-4V tozundan L-PBF prosesi ile dikdörtgen numuneler üretilmiştir. Numunelerin hem üst hem de yan yüzeylerinin yüzey topografisi, yüzey pürüzlülüğü test cihazı ve taramalı elektron mikroskobu (SEM) kullanılarak karakterize edilmiştir. Yüzey pürüzlülüğünün kaynaklarının iki yönelim arasında önemli ölçüde farklılık gösterdiği bulunmuştur. Yan yüzeylerde, pürüzlülük ağırlıklı olarak kısmen erimiş toz partiküllerinin yapışmasından kaynaklanmaktadır. Aksine, üst yüzey pürüzlülüğü çeşitli kusurlardan etkilenir ve yumrulama fenomeni oldukça pürüzlü yüzeyler oluşturmada önemli bir rol oynar.

Alıntı / Cite

Mohagheghi, S., (2025). Characterization of the Surface Topography of the Ti-6Al-4V Alloy Fabricated by Laser Powder Bed Fusion, Journal of Engineering Science and Design, 13(4), 1034-1046.

Yazar Kimliği / Author ID (ORCID Number)	Makale Süreci / Article Process	
S. Mohagheghi, 0000-0001-7574-9276	**Başvuru Tarihi / Submission Date**	26.05.2025
	Revizyon Tarihi / Revision Date	25.08.2025
	Kabul Tarihi / Accepted Date	08.09.2025
	Yayım Tarihi / Published Date	30.12.2025

[*] İlgili yazar / Corresponding author: samira.mohagheghi@istinye.edu.tr, +90-539-687-0659

CHARACTERIZATION OF THE SURFACE TOPOGRAPHY OF THE TI-6AL-4V ALLOY FABRICATED BY LASER POWDER BED FUSION

Samira MOHAGHEGHI[1†]
[1]İstinye University, Faculty of Engineering and Natural Sciences, Department of Mechanical Engineering, İstanbul 34408, Türkiye

Highlights

- Surfaces of Ti-6Al-4V alloy fabricated by laser powder bed fusion process involve distinct defects originating from complex melting, solidification, cooling processes
- The origin of surface roughness on side and top surfaces is dissimilar
- Surface profiles of both orientations are insensitive to the applied variations in the laser scanning speed, within the studied parameters

Purpose and Scope

This study aims to identify and characterize surface features and defects of the additively manufactured Ti-6Al-4V alloy.

Design/methodology/approach

In this study, the laser powder bed fusion process was used to fabricate the samples made of Ti-6Al-4V alloy. Surface roughness tester and scanning electron microscope were used to examine the surface profiles and defects.

Findings

The features and defects on the side and top surfaces of the as-built samples were characterized. The reasons behind the formation of the rough surfaces on side and top are different. It was shown that these process-inherent defects are not sensitive to the applied change in the laser scanning speed, within the studied parameters.

Research limitations/implications

This research draws attention to the fact that additive manufacturing is a complex process wherein many process parameters can affect the surface quality of the parts. Simplified roughness measurements may be misleading, and complementary techniques should be employed to understand the surface defects.

Practical implications

This paper emphasizes on the process-inherent surface defects and features of the additively manufactured parts. The origin, size, and distribution of the defects should be identified, characterized, and accordingly a suitable surface finishing process should be proposed.

Originality

This paper studies an industrially important alloy, Ti-6Al-4V, fabricated by laser powder bed fusion process in terms of surface quality and defect formation resulting from the process.

† Corresponding author: samira.mohagheghi@istinye.edu.tr, +90-539-687-0659

1. Introduction

Additive manufacturing (AM) processes build three-dimensional (3D) components according to digital models by sequentially adding, melting, and solidifying thin layers of material, enabling the production of geometrically complex and customized components. AM is now broadly recognized as a novel paradigm for the design and fabrication of high-performance components. The progress in the field of high-performance lasers, computing and simulations, and improved metal powder feedstocks have positioned AM as a cutting-edge manufacturing technology with widespread industrial recognition, as evidenced by the rapid growth in sales (DebRoy et al., 2018).

AM processes are classified (ASTM F2792) into two groups: Directed Energy Deposition and Laser Powder Bed Fusion (L-PBF) (DebRoy et al., 2018). In Directed Energy Deposition process, focused thermal energy, such as a laser or arc, melts material as it is deposited (Ahn, 2021). Wide range of materials have been manufactured by this technique (Bartels et al., 2025; Çam, 2022; Çam and Günen, 2024; Kocaman et al., 2025; Seow et al., 2019). The L-PBF process is known by various names in literature, including selective laser melting, direct metal laser sintering, and direct metal laser melting (King et al., 2015). L-PBF process is the widespread technology in additive manufacturing of metals and alloys (Gussone et al., 2020; Hecht et al., 2023; Rodríguez-Sánchez et al., 2025). In this technology, thin layers of metallic powder are uniformly spread over a build platform. An energy source, typically a laser or electron beam, is used to selectively fuse the powder. Once a layer is completed, a fresh layer of powder is spread over the solidified surface, and this layer by layer construction continues until the 3D part is fabricated (King et al., 2015).

Despite its technological advancements, as-built parts exhibit poor surface quality. Key surface defects include balling, partially melted particles adhering to surfaces, stair-stepping artifacts, and micro crack networks (Valentinčič et al., 2024). These process-inherent defects lead to high roughness (10 μm ≤ R_a ≤ 30 μm) in as-built state (Zeidler and Böttger-Hiller, 2022). These defects negatively affect functionality of the additively manufactured parts through multiple failure mechanisms such as weakening load-bearing capacity, exceeding acceptable geometric tolerances affecting assembly fit, elevating friction coefficient and accelerating wear, providing crack nucleation sites and hence, triggering fatigue failure (Boban et al., 2022).

Various studies have been performed on characterizing surface topography of the additively manufactured metallic materials, many of which have evaluated the roughness on the top surface of cubic samples (Snyder and Thole, 2020). Prior research identifies key relationships between printing parameters and surface roughness. Low laser power-induced and high scanning speed-induced balling effect were investigated in components fabricated from stainless steel 316L and it was recommended that the increasing the input energy density via increasing laser power, lowering laser scanning speed, or decreasing powder layer thickness will reduce the possibility of occurring balling defect (Gu and Shen, 2009), which in turn will affect the surface roughness of the component. In another study on printing of AlSi10Mg alloy, it was identified that laser scanning speed is the dominant factor influencing surface roughness (Calignano et al., 2013). In Ti-6Al-4V, studies showed that optimizing energy density via higher power, slower laser scanning speed, or smaller hatch spacing reduces roughness by ensuring full melting and minimizing defects like porosity (Cao et al., 2021). The quality of the powder, its size, and particle size distribution may also have an effect on the formation of different defects. For instance, it was shown that larger powder particles result in coarser surface finishes (Chen et al., 2018). In addition, various scanning strategies, such as non-linear scanning strategies may improve surface topography compared to linear strategy (Zhang and Yuan, 2022).

While most of the studies reported a common trend, *i.e.* decreasing the roughness as energy density input increases, some studies indicate that surface roughness does not scale with energy density (Qiu et al., 2015; Snyder and Thole, 2020). Despite many studies in the field of additive manufacturing and unrevealing process parameter effects on the surface finish of the additively manufactured components, there still exists significant challenges in understanding physics of the process. It is reported that over 50 process parameters (see Table 1 in (Spears and Gold, 2016)) exist which impact the ultimate quality of the additively manufactured part (Spears and Gold, 2016). Therefore, further investigations are required to comprehensively analyze the correlation between process control parameters and the surface finish of additively manufactured components, with the aim of optimizing post-processing requirements and enhancing their performance.

This study investigates the surface features and defects of the Ti-6Al-4V samples fabricated by the L-PBF process. Titanium and titanium-based alloys are employed in the biomedical industry for the fabrication of implants thanks to their excellent biocompatibility, high corrosion resistance, and superior mechanical properties (Çam et al., 2006; Osman RB and MV., 2015; Silva et al., 2022). In such applications, surface quality plays a crucial role in overall performance of the part. To vary volumetric energy density, three laser scanning speeds are applied, while other parameters were kept constant. The roughness measurements and topography analyses were conducted

using a roughness measurement tester and a scanning electron microscope (SEM), respectively. Various surface features and defects were identified and characterized. It is shown that, within the studied process parameters, the applied laser scanning speed variations do not significantly affect the quality of both side and top surfaces. The magnitudes of the R_a value, the arithmetic average of the absolute deviations of surface heights from the mean line, is relatively homogenous on the side surfaces and the main origin of the roughness on these surfaces is partially melted powder adhering to the hot surface during layer-by-layer construction of the samples. This finding is well supported by the SEM examinations of the surfaces. In contrast, the origin of the roughness on the top surface is multiple and more complex. The laser tracks, splashed powder from other samples, and the balling defects are the main reasons of the rough top surfaces. Among these, the balling defect, characterized by its size and shape, lead to highly rough and irregular surfaces restricting the roughness measurements.

2. Material and Method

2.1. Material

The Ti-6Al-4V powder was supplied from NANOVAL GmbH & Co. KG. The powder was produced by the gas atomization process. The average particle size of the powder is 47.0 µm. The particle size distribution of the powder is shown in Figure 1 (a). The distribution is relatively narrow, suggesting good control over powder size, which is important for consistent layer spreading and melting during the L-PBF process. Figure 1 (b) represents the SEM image of the used Ti-6Al-4V powder. The particles are predominantly spherical, which is ideal for the L-PBF process as it promotes good flowability and packing density. The chemical composition of the bar samples before atomization measured according to ASTM E2371-13 by the supplier is given in Table 1. The Ti-6Al-4V powder consists primarily of titanium, with aluminum and vanadium contents. This composition conforms to the standard specification for Ti-6Al-4V alloy commonly used in additive manufacturing.

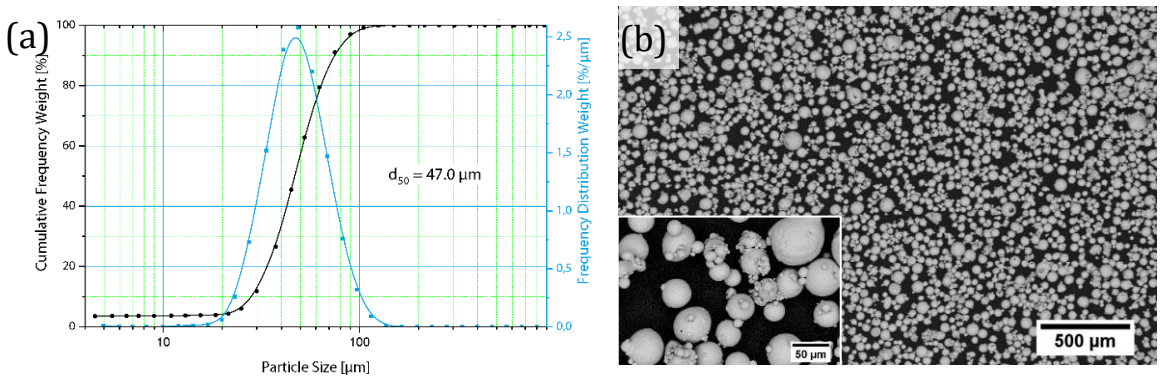

Figure 1. (a) Particle size distribution of the Ti-6Al-4V powder. (b) The SEM image of the Ti-6Al-4V powder. The inset shows the powder at a high magnification. The images demonstrate an even distribution of particle sizes, consistent with the measured distribution in (a).

Table 1. The composition of the used Ti-6Al-4V powder, provided by the supplier.

Element	Ti	Al	V	Fe	C	N	O	H
wt.%	Base	6.36	4.23	0.210	0.010	0.007	0.105	0.0006

2.2. Method

The samples were fabricated using an Aconity MINI L-PBF system in Access e.V. (Sizova et al., 2021). The system is equipped with a 400 W single-mode laser. The spot size of the laser beam is approximately 80 µm and laser wavelength is 1070 nm. The build platform was unheated. The L-PBF process was carried out under a high-purity argon gas, with a residual oxygen content less than 200 ppm, which ensures minimal oxidation during processing. Rectangular samples, having a cross-section of 5 mm × 20 mm and a height of 7.6 mm, were manufactured. An image of the L-PBF process in the current study is shown in Figure 2 (a). A bidirectional simple scanning strategy was used. The orientation of the scan vectors was rotated by 67° between successive layers. The schematic of the scanning strategy is shown in Figure 2 (b). The experiments were performed using the following parameters: laser power of 100 W, hatch distance of 0.08 mm, and layer thickness of 0.03 mm, while three laser scanning speeds of 950, 1000, 1050 mm/s were applied.

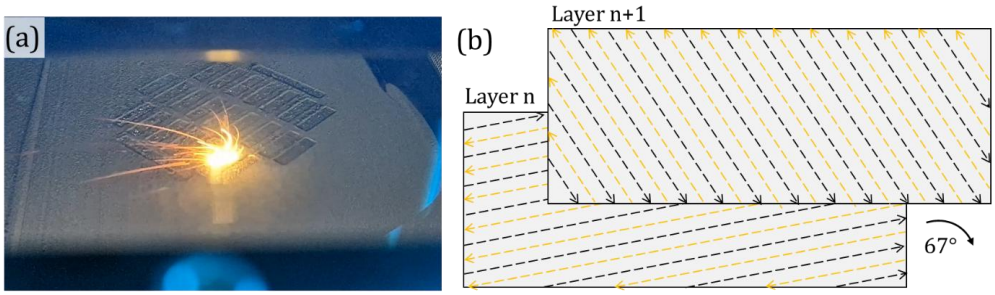

Figure 2. (a) Image of the L-PBF process. (b) Schematic of the printing strategy showing 67 degrees rotation of the scan vector between each successive layer.

In some of the samples, a contour, i.e., melting the outer perimeter of a part's cross-section in each layer, is applied. The printing parameters of the contour were the same as the sample, with offset of the contour of 0.1 mm.

To calculate the volumetric energy density, the following equation was used and the results are tabulated in Table 2, along with sample names used in this study.

$$E_{L\text{-}PBF} = \frac{P}{\nu . \ h . \ t}$$

In this equation, P, ν, h, and t are the laser power, the laser scanning speed, the hatch distance, and the layer thickness, respectively. The image of the fabricated rectangular samples viewed from the build direction on the build plate is given in Figure 3 (a). Sample geometry for 23 samples is given in Figure 3 (b). Two larger rectangular samples are also fabricated (T1* and T25).

Table 2. L-PBF process parameters of the Ti-6Al-4V samples.

Sample name	Laser power (W)	Laser scanning speed (mm/s)	Energy density (J/mm³)
T1*-T2*-T3*-T4*-T5*-T6-T7-T8	100	1000	41.7
T9*-T10*-T11*-T12*-T13*-T14-T15-T16-T17	100	950	43.9
T18*-T19*-T20*-T21*-T22-T23-T24-T25	100	1050	39.7

The * sign represents the samples with contour.

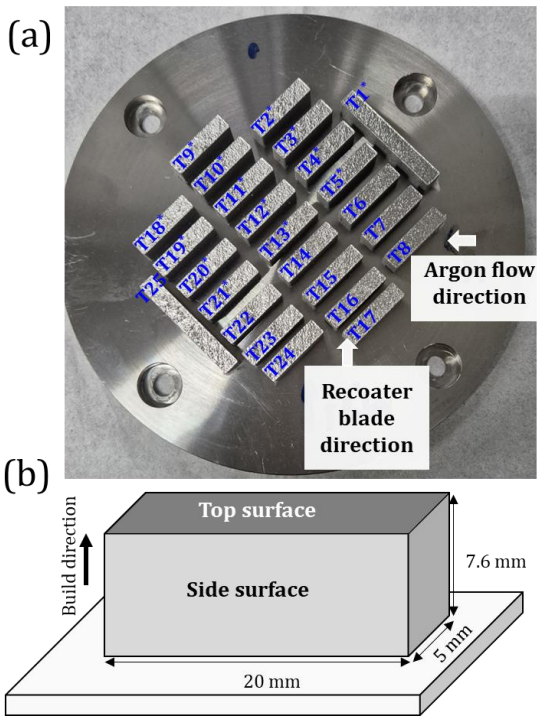

Figure 3. (a) As-built Ti-6Al-4V samples viewed from the build direction. The direction of the blade movement, and hence the powder spread, is given along with the direction of argon flow. (b) The drawing of the rectangular samples. Top and side surfaces are shown.

2.3. Test and Analysis

For quantification of the surface roughness, Mitutoyo SURFTEST SJ-210 portable surface roughness tester with a maximum range of 360 μm (-200 μm to +160 μm) was used. The tester is equipped by a stylus with diamond tip radius of 2 μm. The measuring force is 0.75 mN, and travel speed is 0.5 mm/s. To determine the roughness, the primary profile is filtered (Gaussian filter according to ISO 1997) to remove the waviness of the profile. The cutoff length, λs (short-wavelength filter) and λc (long-wavelength filter) are 2.5 and 0.8 mm, respectively. The 2-dimensional height profile of a line scan was recorded for each sample and plotted. In this study R_a, which is the arithmetic mean of the absolute values of the surface height deviations from a mean line calculated over a specified length, is considered as the main roughness parameter. In addition, R_q and R_z are reported—representing the root mean square of the surface height deviations from the mean line, and the average vertical distance between the five highest peaks and five deepest valleys, respectively. The evaluation length is 4 mm and three measurements per sample were performed on the side surface. These three measurements were taken along the same stylus scanning direction but at different locations on a given side surface. The average and standard deviation of the three measurements were presented.

Zeiss Scanning Electron Microscope (ULTRA55), equipped with a Gemini field emission column were used for surface characterization of the samples.

3. Result and Discussion

3.1. Quantification of the Surface Roughness

The roughness measurements show clear differences between side and top surfaces. While the side surfaces displays a relatively homogenous roughness values, top surfaces have very nonhomogeneous profiles which essentially depends on the existence of different surface defects. Surface defects at both surfaces will be discussed in detail in section 3.2. Figure 4 (a) and (b) show examples of the surface profiles measured from side surfaces of sample T7 and T1*, respectively. These two samples are fabricated with the same process parameters with a difference in applying contour in T1*. The graphs display height variations across the measured length of 4 mm, with peaks reaching around +40 μm and valleys extending to about -30 μm in (a) and peaks of about +40 μm and valleys extending to about -50 μm in (b). The applied contour in T1* does not affect the surface quality in terms of the surface profile shape, as evidenced by comparing Figure 4 (a) and (b). Numerous peaks and valleys that are characteristic of the surface of metallic materials fabricated by additive manufacturing processes can be seen. The three measurements of all samples show no clear trend of surface quality deterioration or improvement across the measured lengths, suggesting consistent processing was maintained during fabrication.

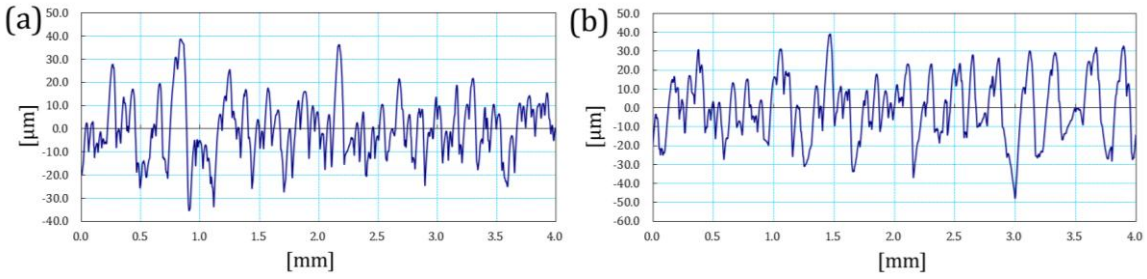

Figure 4. Side surface profiles of the (a) sample T7 without counter and (b) sample T1* with a counter.

The detail of the surface roughness measurements is tabulated in Table 3 and illustrated in Figure 5. A strong positive correlation exists between three roughness parameters, as expected. Overall measurements suggest that the applied variation in the laser scanning speed and consequently, the energy density, does not affect the roughness values significantly. Figure 5 shows the distribution of the R_a as a function of laser scanning speeds, ranging from 10.659 μm in sample T7 to 15.000 μm in sample T24. These values suggest that within the studied parameters, the powder particle size has a determining effect on the magnitude of the side surface roughness. The used powder had d_{50}= 47 microns. This essentially indicates that 50% of the powder particles are smaller than 47 microns and 50% are larger. The surface profiles shown in Figure 4 can be closely correlated to the powder size distribution. The applied counter strategy is found to be ineffective, with no measurable effect on the roughness.

Table 3. Comprehensive surface roughness measurements for 25 samples manufactured by L-PBF process.

Sample name	R_a (um)	R_q (um)	R_z (um)	Sample name	R_a (um)	R_q (um)	R_z (um)
T1*	12.349	15.169	66.072	T14	11.296	14.062	63.217
T2*	11.231	14.019	65.603	T15	13.241	16.332	70.788
T3*	12.660	15.543	68.405	T16	14.056	17.286	76.641
T4*	12.554	15.006	64.425	T17	11.158	13.713	60.357
T5*	11.815	14.586	64.972	T18*	13.015	16.083	71.176
T6	11.150	14.001	64.484	T19*	12.479	15.254	67.157
T7	10.659	13.224	60.704	T20*	11.731	14.332	64.061
T8	13.060	15.860	69.032	T21*	11.833	14.486	63.273
T9*	12.998	15.712	66.502	T22	13.306	16.432	71.902
T10*	13.214	16.464	74.020	T23	12.199	14.978	66.434
T11*	11.685	14.469	66.396	T24	15.000	18.242	79.131
T12*	12.178	14.811	70.459	T25	10.678	13.291	60.572
T13*	12.041	14.764	63.826				

The *sign represents the samples with contour.

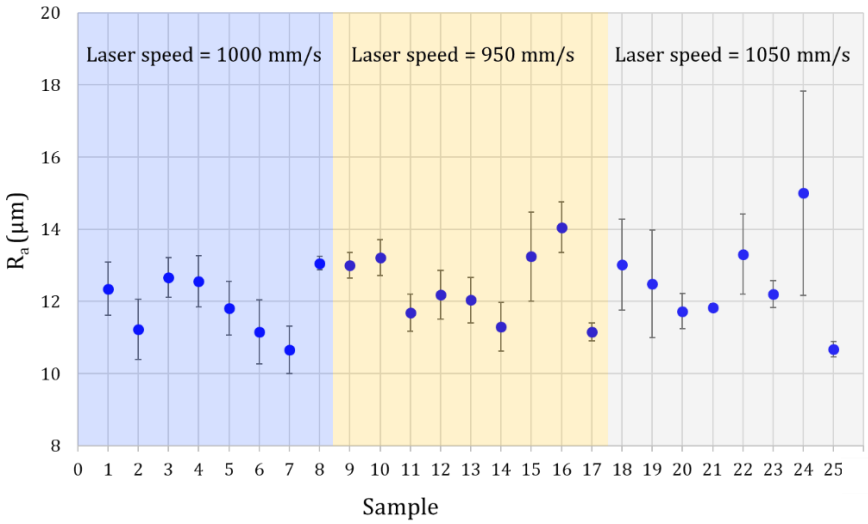

Figure 5. The arithmetic average roughness (R_a) values of the side surfaces of 25 samples. The R_a was measured three times per sample and the average with the standard deviation was reported for each sample.

The local defects introduce considerable variability and can mask subtle changes in roughness that might otherwise be attributed to processing conditions. Therefore, relying solely on R_a could lead to misleading conclusions regarding the relationship between process parameters and surface quality. In fact, the process parameters must influence the defect types and magnitude. However, within the employed scanning speeds, this variation does not substantially change the type and magnitude of the defects.

In contrast to the side surfaces, the top surfaces display non-uniform roughness that is primarily influenced by the local defects. In regions where significant surface defects are absent, surface roughness measurements can be performed. Within these areas, the R_a values are lower than those observed on the side surfaces. Therefore, the origin of the roughness should be different than the one on the side surfaces. This roughness in this case is generated by the laser tracks and will be discussed in detail in section 3.2. However, in zones where large defects are present, the roughness values are excessively high, making it impossible to obtain accurate measurements with the current device. Firstly, similar to the side surfaces, there is no clear trend in the magnitude of R_a as a function of the laser scanning speed. This suggests that applied scanning speeds, *i.e.*, 950, 1000, 1050 mm/s, do not systematically influence the average surface roughness. Secondly, it is important to emphasize that the presence of local defects significantly affects the surface profile. As a result, R_a may not be a reliable parameter for correlating process parameters, such as laser scanning speed, to surface roughness. Utilizing non-contact instrument, like white light interferometry and 3D optical surface profilometry, can be helpful to capture the representative surface profiles. In particular, on curved surfaces, the use of a short evaluation length in contact-based measurements may lead to unrepresentative results, potentially obscuring the true origin of surface

roughness in additively manufactured parts (Poyraz et al., 2019). On the other hand, in the presence of local defects, employing non-contact measurement techniques may still result in unrepresentative surface roughness. This deviation does not arise from the limitations of the measurement method itself but rather from the inherent nature of the defect. Hence, correlating process parameters to surface roughness remains challenging.

Figure 6 (a) presents the R_a values measured from the top surfaces, specifically in regions where large defects are absent or minimal. For example, the surface profile of the sample with the lowest R_a value, designated as T4*, is illustrated in Figure 6 (b). This profile demonstrates no abrupt changes that would indicate the presence of local defects. In contrast, sample T13*, which exhibits the highest measurable R_a value, displays a pronounced local and large peak and valley in its surface profile (shown by the red arrow in Figure 6 (c)) clearly pointing to the presence of a large but measurable defect in that area.

These observations highlight the substantial impact that local defects have on surface roughness measurements. On top surfaces, while large defect-free regions tend to yield low and more consistent R_a values, the presence of even a single defect can dramatically increase R_a and distort the overall assessment of surface quality. This underscores the importance of carefully selecting measurement locations and considering the influence of localized imperfections when interpreting roughness data and evaluating process parameters.

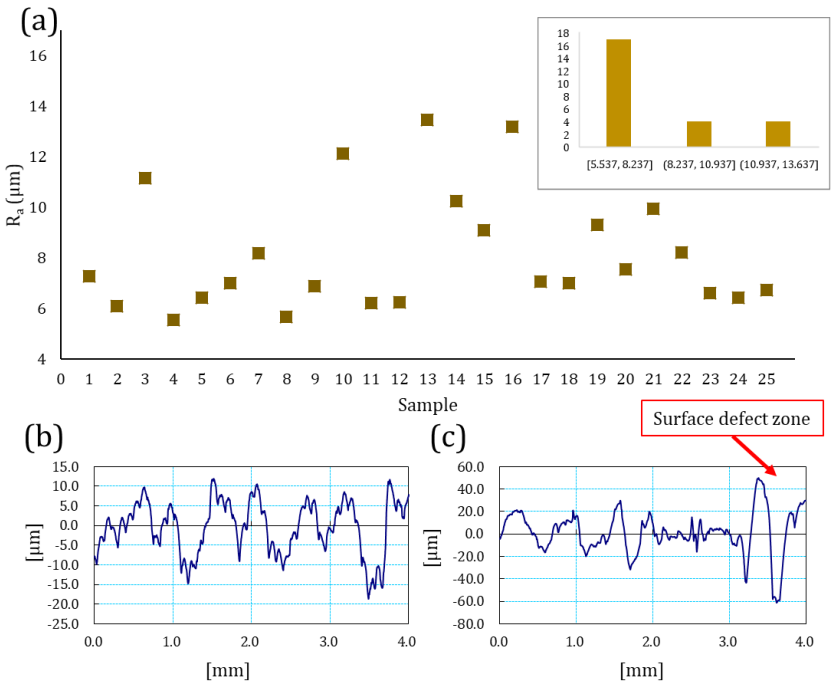

Figure 6. (a) The R_a values of the top surfaces from the locations wherein the large defects are absent or minimal. The inset is showing a histogram where the most measured R_a values are ranged between approximately 5 - 8 µm (b) The surface profile of sample T4* having minimum R_a value (c) Surface profile of the T13* having maximum measured R_a value. The red arrow shows a region where a large defect is present.

3.2. Investigation of the Surface Topography by Scanning Electron Microscope

Surface of the samples fabricated by the L-PBF process can appear in various forms, each distinguished by its unique length scales and shapes. Characterizing these surface features is essential for analyzing and optimizing the L-PBF process parameters. In particular, as it was shown in previous section, the surface roughness value may lead to misunderstanding of the relation between the L-PBF process parameters and the surface quality of the additively manufactured parts.

Origin of roughness in side and top surfaces are found to be entirely dissimilar. The side surfaces in all samples, irrespective of the variation in the laser scanning speed, involving partially melted powder particles that are adhered to the surface. This defect is a result of having extremely hot as-solidified surfaces in contact with un-melted neighboring powder. As the region around the laser pass melts and solidifies, the neighboring powder adheres to the hot surface (Snyder and Thole, 2020), and this leads to the formation of rough surfaces.

The SEM images in Figure 7 (a) and (b) show the side surfaces of the rectangular sample T11* and T16, revealing several characteristic side surface features of L-PBF-manufactured components. The most prominent feature is

the extensive presence of partially melted powder particles adhered to the surface. These spherical particles appear in various sizes but are consistent with the size distribution of the used powder. In other words, the size distribution of these particles corresponds to the powder size range used in the L-PBF process. The spatial distribution of these partially melted powders is non-periodic, indicating the random nature of particle adhesion during fabrication (Liu et al., 2024). It should be noted that sample T11* has a counter while T16 does not have. There are not any significant differences in the surface features of these two samples pointing to insignificant improvement, if any, by applying the current counter strategy. The surface profile of these samples are given in Figure 7 (c) and (d) with the R_a values of 11.685 and 14.056 µm for T11* and T16 samples, respectively. The surface profile patterns in Figure 7 (c) and (d) with numerous peaks and valleys correspond directly to the surface features visible in the SEM image in Figure 7 (a) and (b), where peaks represent protruding particles and valleys indicate spaces between particles.

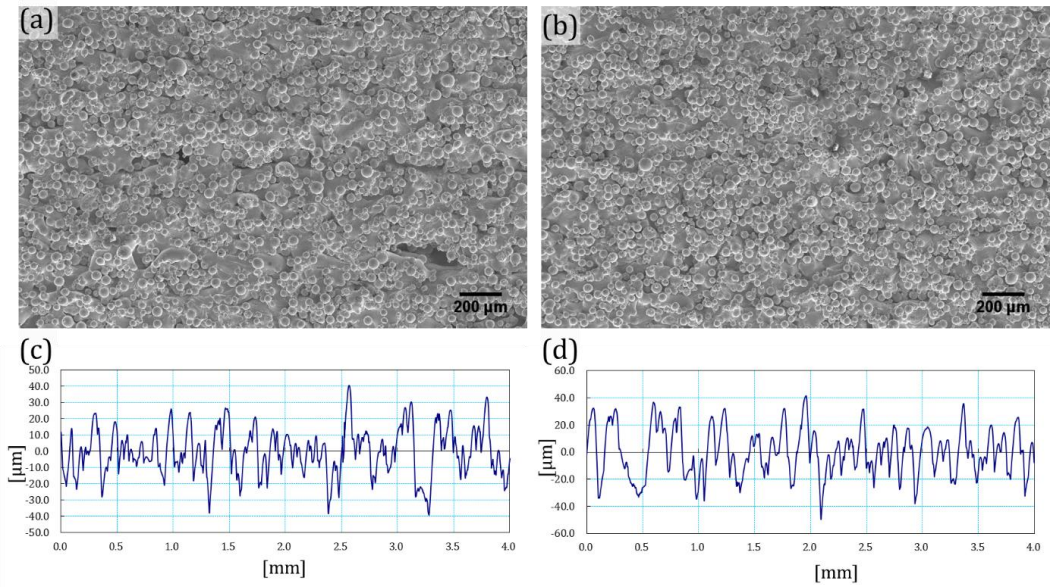

Figure 7. SEM images in (a) and (b) are showing the side surfaces of the rectangular samples T11* and T16, respectively. (a) Surface profile of the sample T11*. (b) Surface profile of the sample T16.

Figure 8 provides a high-magnification view of the side surface from sample T20*. The image reveals several characteristic features of L-PBF-processed surfaces; in addition to numerous spherical particles of varying diameters adhered to the surface, representing partially melted powder particles, some small voids and gaps are visible at the junctions, which may be the result of the incomplete melting that occurs at the periphery of melt pools during L-PBF processing. These may represent lack-of-fusion defects and contribute to the overall surface roughness. The underlying surface shows evidence of melt pool formation and solidification with some visible flow patterns.

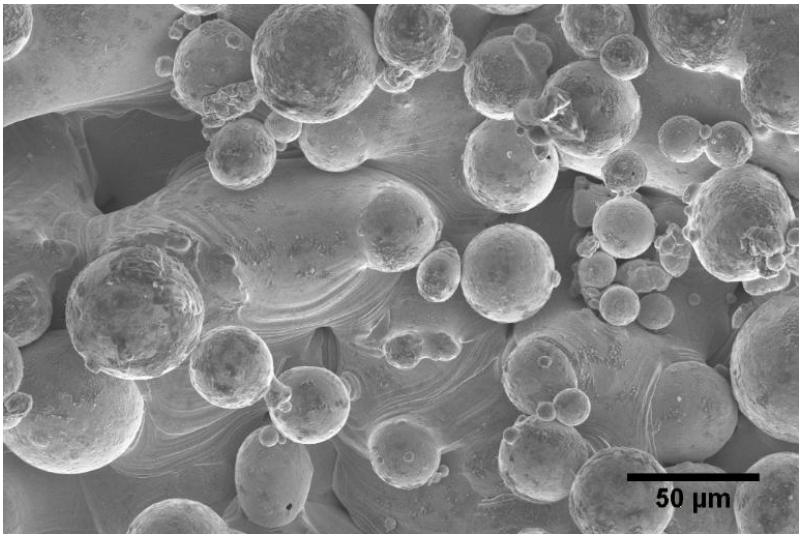

Figure 8. High magnification view of the side surface, illustrating the partially melted powder particles adhering to the surface. A lack-of-fusion defect is visible in the upper left corner of the image.

Figure 9 (a) and (b) show characteristic top surface topographies observed in the as-built samples. The samples in Figure 9 (a) and (b) were fabricated with and without contour, respectively, as evidenced by the horizontal region separated from the angular laser tracks in Figure 9 (a). In both images, laser scanning tracks are clearly visible, separated by parallel lines, which are the main origin of the surface roughness of the top surfaces in regions wherein other defects are absent or minimal. The surfaces exhibit clear evidence of overlapping melt pools. In addition, several partially-melted powder particles adhering to the surface can be seen, shown by yellow arrows. These powder particles were splashed from the neighbor samples during printing process. Similar to the side surfaces, the applied differences in the laser scanning speed does not impact the surface topography, significantly.

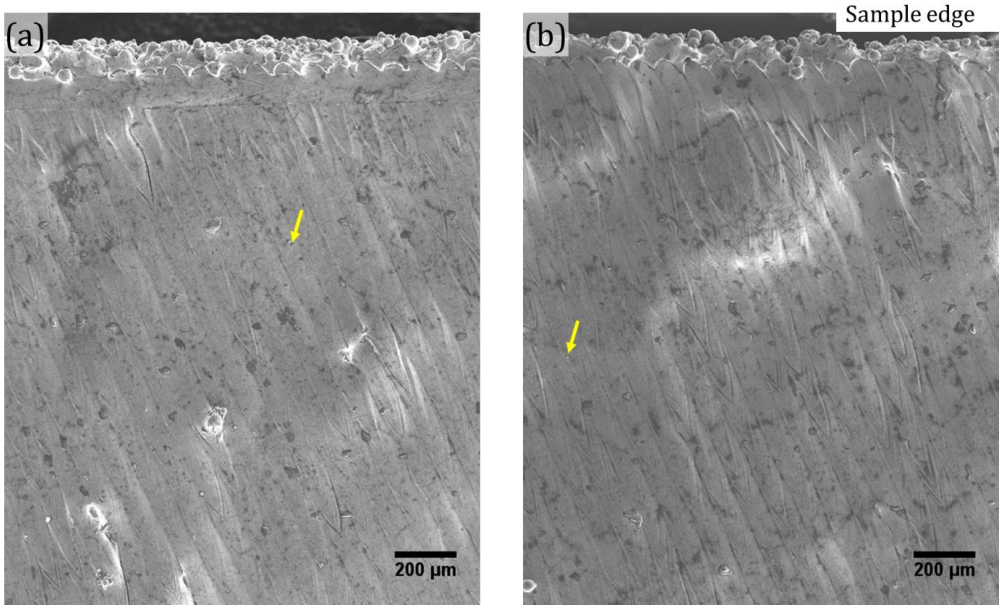

Figure 9. SEM images showing the characteristic top surface topographies of the (a) sample T4* with counter (b) sample T7 without counter. Laser scan tracks are visible as parallel inclined columns.

The visible directional solidification patterns within the melt tracks indicates the cooling direction in the process. These patterns are better resolved in Figure 10 (a). The surface profile of this sample is given in Figure 10 (b). This measurement was performed in the region where large defects are absent. Therefore, the origin of the roughness with R_a value of 7.543 µm, (given in Figure 6), is mainly related to the scan tracks seen in the image. Small defects on the surface, likely splashed droplet/powder, lead to the peaks observed in the surface profile.

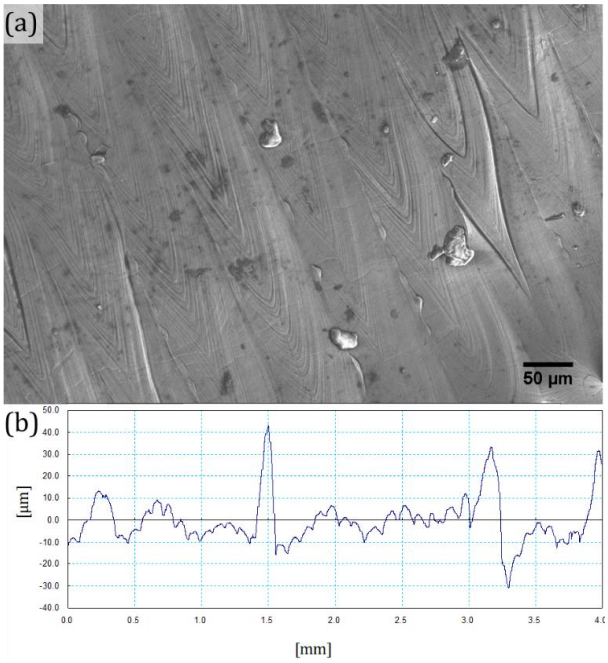

Figure 10. (a) As-built top surface of sample T11*. Characteristic laser scan tracks form as the laser melts the powder and the subsequently solidification occurs. There are few solidified droplets on the surface. (b) Surface profile of the relatively defect-free area on the top surface of the same sample. Peaks seen in the graph correspond to local defects.

The major defect observed on the top surface is large semi-spherical defects (>100 μm) protruding from the surface, which represent "balling" defects. Balling is a phenomenon characterized by the formation of spherical droplets rather than continuous melt tracks during the laser melting process in L-PBF. Balling is a common defect observed in laser powder bed fusion process, and is caused by instabilities in the melt pool (Tolochko et al., 2004). This phenomenon can occur at both low laser energy levels, where incomplete wetting prevents proper fusion, and at high laser energy levels, where excessive heat causes the molten metal to splash onto surrounding region, leading to the formation of spherical droplets on the surface (Gu and Shen, 2009).

An example of the balling defects is shown in Figure 11. In the image, the semi-spherical shaped protrusions along the melt pool tracks are a direct manifestation of this defect. The size of these defects, approximately 350 μm, confirms that these features are much larger than typical powder particles, further supporting that these are not partially melted powder but rather solidified droplets formed during printing. These large defects caused large peak values of the surface profile. Indeed, in the zones where these defects are present, the roughness values reported in Figure 6 are no longer applied.

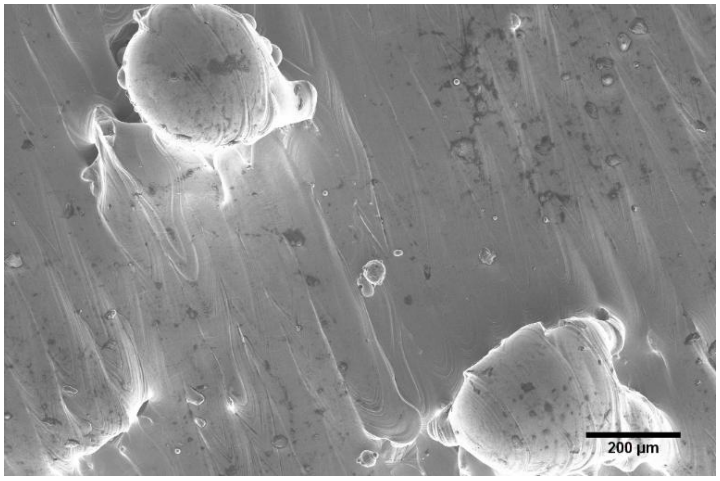

Figure 11. Example of the balling defect formed on the top surface of sample T23.

4. Summary and Conclusion

In summary, laser powder bed fusion (L-PBF) inherently produces a variety of surface features and defects. These features arise from the complex interplay of thermal gradients, melt pool dynamics, and powder characteristics during the layer-by-layer fabrication process, and typically result in rough as-built surfaces. While systematic optimization of process parameters can significantly reduce the prevalence and severity of these defects, complete elimination remains challenging. Even with advanced parameter tuning, certain imperfections persist due to the fundamental physics of the process, the stochastic nature of powder adhesion, and melt pool instabilities.

The origins of the roughness are shown to be different on side and top surfaces. The primary contributor to the roughness on side surfaces of the Ti-6A-4V fabricated by L-PBF is the adherence of partially melted powder particles. It is shown that the size and distribution of these particles closely match with the initial powder, indicating that powder characteristics play a determining role in side surface roughness. SEM images confirmed the prevalence of these particles and the lack of significant improvement from applying the current contour scan strategy. On the other hand, the top surfaces topography is more complex and heterogeneous, arising from multiple features including laser scanning tracks, splashed powder, and especially “balling” defects. In regions of the top surfaces free from major defects, the R_a values were lower than the side surfaces and more consistent, but the presence of even a single large defect could result in excessively high roughness, beyond the measurement capability of the used tester. Within the range of laser scanning speeds (950, 1000, 1050 mm/s), there was no significant effect on the surface R_a for either the side or top surfaces.

This study highlights that relying solely on R_a as a metric can be misleading, especially for top surfaces where the local defects dominate with multiple origins, and thus size, distribution, and shape. The presence or absence of such defects can mask subtle effects of process parameters, underscoring the need for careful selection of measurement locations and complementary qualitative analyses.

These findings emphasize the importance of characterizing the surface defects and suggest the necessity of the surface post-processing techniques. Therefore, even with the full process optimization, which may not be even feasible considering the role of about 50 parameters at play, exploring effective post-processing methods is

essential for meeting the strict surface quality requirements of advanced technological applications, particularly in aerospace and biomedical sectors.

Acknowledgement

This work was supported by the Alexander von Humboldt Foundation (www.humboldt-foundation.de). The author would like to thank the team in Access e.V. (https://access-technology.de/) to assist the author to perform 3D-printing and sample characterizations.

Conflict of Interest

No conflict of interest was declared by the author.

References

Ahn, D.-G., 2021. Directed Energy Deposition (DED) Process: State of the Art. International Journal of Precision Engineering and Manufacturing-Green Technology, 8, 703-742.

Bartels, D., Nikas, D., März, R., Marschall, M., Schrauder, J., Merklein, M., Şelte, A., & Krakhmalev, P., 2025. Directed energy deposition of chromium-molybdenum-vanadium cold work tool steel Vanadis 4 Extra©. Journal of Materials Research and Technology, 38, 1573-1580.

Boban, J., Ahmed, A., Jithinraj, E. K., Rahman, M. A., & Rahman, M., 2022. Polishing of additive manufactured metallic components: retrospect on existing methods and future prospects. The International Journal of Advanced Manufacturing Technology, 121, 83-125.

Calignano, F., Manfredi, D., Ambrosio, E. P., Iuliano, L., & Fino, P., 2013. Influence of process parameters on surface roughness of aluminum parts produced by DMLS. The International Journal of Advanced Manufacturing Technology, 67, 2743-2751.

Çam, G., 2022. Prospects of producing aluminum parts by wire arc additive manufacturing (WAAM). Materials Today: Proceedings, 62, 77-85.

Çam, G., & Günen, A., 2024. Challenges and opportunities in the production of magnesium parts by directed energy deposition processes. Journal of Magnesium and Alloys, 12, 1663-1686.

Çam, G., İpekoğlu, G., Bohm, K. H., & Koçak, M., 2006. Investigation into the microstructure and mechanical properties of diffusion bonded TiAl alloys. Journal of Materials Science, 41, 5273-5282.

Cao, S., Zou, Y., Lim, C. V. S., & Wu, X., 2021. Review of laser powder bed fusion (LPBF) fabricated Ti-6Al-4V: process, post-process treatment, microstructure, and property. Light: Advanced Manufacturing, 2, 313-332.

Chen, Z., Wu, X., Tomus, D., & Davies, C. H. J., 2018. Surface roughness of Selective Laser Melted Ti-6Al-4V alloy components. Additive Manufacturing, 21, 91-103.

DebRoy, T., Wei, H. L., Zuback, J. S., Mukherjee, T., Elmer, J. W., Milewski, J. O., Beese, A. M., Wilson-Heid, A., De, A., & Zhang, W., 2018. Additive manufacturing of metallic components – Process, structure and properties. Progress in Materials Science, 92, 112-224.

Gu, D., & Shen, Y., 2009. Balling phenomena in direct laser sintering of stainless steel powder: Metallurgical mechanisms and control methods. Materials & Design, 30, 2903-2910.

Gussone, J., Bugelnig, K., Barriobero-Vila, P., da Silva, J. C., Hecht, U., Dresbach, C., Sket, F., Cloetens, P., Stark, A., Schell, N., Haubrich, J., & Requena, G., 2020. Ultrafine eutectic Ti-Fe-based alloys processed by additive manufacturing – A new candidate for high temperature applications. Applied Materials Today, 20, 100767.

Hecht, U., Vayyala, A., Barriobero-Vila, P., Navaeilavasani, N., Gein, S., Cazic, I., & Mayer, J., 2023. Microstructure evolution in the hypo-eutectic alloy Al0.75CrFeNi2.1 manufactured by laser powder bed fusion and subsequent annealing. Materials Science and Engineering: A, 862, 144315.

King, W. E., Anderson, A. T., Ferencz, R. M., Hodge, N. E., Kamath, C., Khairallah, S. A., & Rubenchik, A. M., 2015. Laser powder bed fusion additive manufacturing of metals; physics, computational, and materials challenges. Applied Physics Reviews, 2,

Kocaman, E., Gürol, U., Günen, A., & Çam, G., 2025. Effect of post-deposition heat treatments on high-temperature wear and corrosion behavior of Inconel 625. Materials Today Communications, 42, 111101.

Liu, J., Zhao, K., Wang, X., & Li, H., 2024. Effect of Initial Surface Morphology and Laser Parameters on the Laser Polishing of Stainless Steel Manufactured by Laser Powder Bed Fusion. Materials, 17, 4968.

Osman RB, & MV., S., 2015. A critical review of dental implant materials with an emphasis on titanium versus zirconia. Materials 8(3), 932-958.

Poyraz, Ö., Solakoğlu, E. U., Ören, S., Tüzemen, C., & Akbulut, G., 2019. Toz yatağı katmanlı imalat prosesinde yüzey dokusu ve form karakterizasyonu. Gazi Üniversitesi Mühendislik Mimarlık Fakültesi Dergisi, 34, 1653-1664.

Qiu, C., Panwisawas, C., Ward, M., Basoalto, H. C., Brooks, J. W., & Attallah, M. M., 2015. On the role of melt flow into the surface structure and porosity development during selective laser melting. Acta Materialia, 96, 72-79.

Rodríguez-Sánchez, M., Boccardo, A. D., Sadanand, S., Ghavimi, A., Busch, R., Sharangi, P., Ferrara, E., Barrera, G., Tiberto, P., Tourret, D., Gallino, I., & Pérez-Prado, M. T., 2025. Laser powder bed fusion of an Fe-based metallic glass using time delays. Additive Manufacturing, 110, 104922.

Seow, C. E., Coules, H. E., Wu, G., Khan, R. H. U., Xu, X., & Williams, S., 2019. Wire + Arc Additively Manufactured Inconel 718: Effect of post-deposition heat treatments on microstructure and tensile properties. Materials & Design, 183, 108157.

Silva, R. C. S., Agrelli, A., Andrade, A. N., Mendes-Marques, C. L., Arruda, I. R. S., Santos, L. R. L., Vasconcelos, N. F., & Machado, G., 2022. Titanium dental implants: an overview of applied nanobiotechnology to improve biocompatibility and prevent infections. Materials, 15, 3150.

Sizova, I., Sviridov, A., Bambach, M., Eisentraut, M., Hemes, S., Hecht, U., Marquardt, A., & Leyens, C., 2021. A study on hot-working as alternative post-processing method for titanium aluminides built by laser powder bed fusion and electron beam melting. Journal of Materials Processing Technology, 291, 117024.

Snyder, J. C., & Thole, K. A., 2020. Understanding Laser Powder Bed Fusion Surface Roughness. Journal of Manufacturing Science and Engineering, 142,

Spears, T. G., & Gold, S. A., 2016. In-process sensing in selective laser melting (SLM) additive manufacturing. Integrating Materials and Manufacturing Innovation, 5, 16-40.

Tolochko, N. K., Mozzharov, S. E., Yadroitsev, I. A., Laoui, T., Froyen, L., Titov, V. I., & Ignatiev, M. B., 2004. Balling processes during selective laser treatment of powders. Rapid Prototyping Journal, 10, 78-87.

Valentinčič, J., Koroth, J. E., & Zeidler, H., 2024. Advancements in surface finish for additive manufacturing of metal parts: a comprehensive review of plasma electrolytic polishing (PEP). Virtual and Physical Prototyping, 19, e2364222.

Zeidler, H., & Böttger-Hiller, F., 2022. Plasma-electrolytic polishing as a post-processing technology for additively manufactured parts. Chemie Ingenieur Technik, 94, 1024-1029.

Zhang, T., & Yuan, L., 2022. Understanding surface roughness on vertical surfaces of 316 L stainless steel in laser powder bed fusion additive manufacturing. Powder Technology, 411, 117957.